

Acknowledgements

We thank B.-A. Bjerke and C. K. Aas for assistance, and T. Amundsen, M. Andersson, T. R. Birkhead, D. Blomqvist, L. T. T. Hansen, B. Kempnaers, F. Mehlum, M. Petrie and T. Slagsvold, for comments. This work was supported by a post-doc fellowship from the Norwegian Research Council (A.J.) and a grant from the Nansen Endowment (J.T.L.). Permission to carry out the immune experiment on nestling bluethroats was given by the Norwegian Animal Research Authority.

Correspondence and requests for materials should be addressed to J.T.L. (e-mail: j.t.lifjeld@toyen.uio.no).

Magnetite defines a vertebrate magnetoreceptor

Carol E. Diebel*†, Roger Proksch‡§, Colin R. Green||, Peter Neilson‡ & Michael M. Walker*

* Experimental Biology Research Group, School of Biological Sciences, University of Auckland, Private Bag 92019, Auckland, New Zealand

‡ Magnetism Laboratory, Digital Instruments, Santa Barbara, California 93117, USA

|| Department of Anatomy with Radiology, School of Medicine, University of Auckland, Private Bag 92019, Auckland, New Zealand

The key behavioural, physiological and anatomical components of a magnetite-based magnetic sense have been demonstrated in rainbow trout (*Oncorhynchus mykiss*)¹. Candidate receptor cells located within a discrete sub-layer of the olfactory lamellae contained iron-rich crystals that were similar in size and shape to magnetite crystals extracted from salmon^{1,2}. Here we show that these crystals, which mapped to individual receptors using confocal and atomic force microscopy, are magnetic, as they are uniquely associated with dipoles detected by magnetic force microscopy. Analysis of their magnetic properties identifies the crystals as single-domain magnetite. In addition, three-dimensional reconstruction of the candidate receptors using confocal and atomic force microscopy imaging confirm that several magnetic crystals are arranged in a chain of about 1 µm within the receptor, and that the receptor is a multi-lobed single cell. These results are consistent with a magnetite-based detection mechanism^{2,3}, as 1-µm chains of single-domain magnetite crystals are highly suitable for the behavioural and physiological responses to magnetic intensity previously reported in the trout.

Permanently magnetized single-domain magnetite crystals ('lodestone', Fe-O Fe₂O₃) have been described in many different phyla², and the suitability of magnetite for magnetoreception has been analysed in detail²⁻⁵. If the crystals in the nose of the trout are single-domain magnetite, they could act as detector elements within a receptor if their movement, or the torque on them, arising from the interaction of their magnetic moments with the earth's magnetic field is measurable by the nervous system⁶. Single 50-nm crystals of magnetite do not interact strongly enough with the earth's magnetic field to overcome the randomizing effects of thermal buffeting²; however, if the crystals are arranged in chains as in the magnetotactic bacteria, their individual moments will sum linearly. The average orientation of a freely rotating chain will be aligned with the external field vector, whereas the variance of the chain's orientation will depend on the intensity of the external field. Chains of crystals with magnetic-to-thermal energy ratios of two and six are optimal for detecting magnetic intensity and direction,

respectively². A consistent chain length giving either of the above ratios will thus provide evidence of selection for use of the chains in magnetoreception.

The existence of magnetite-based receptors is difficult to demonstrate because the magnetite crystals are too small to be detected easily and the receptors do not need to be aggregated into a complex sense organ^{1,7}. We previously imaged putative magnetite crystals in thin sections from the nose of the trout but were unable to identify the crystals uniquely nor show that the crystals were organized for use in magnetoreception¹. To overcome the problems of scale presented by the small size and low volume concentrations of the crystals, we have now combined confocal laser scanning microscopy (CLSM) with atomic force microscopy (AFM)/magnetic force microscopy (MFM) techniques to characterize the putative magnetite crystals and the candidate magnetoreceptor cells in the trout.

Magnetic force microscopy is capable of determining magnetic domain structure in a variety of magnetic materials, including small particles with a spatial resolution of less than 100 nm. Because it is

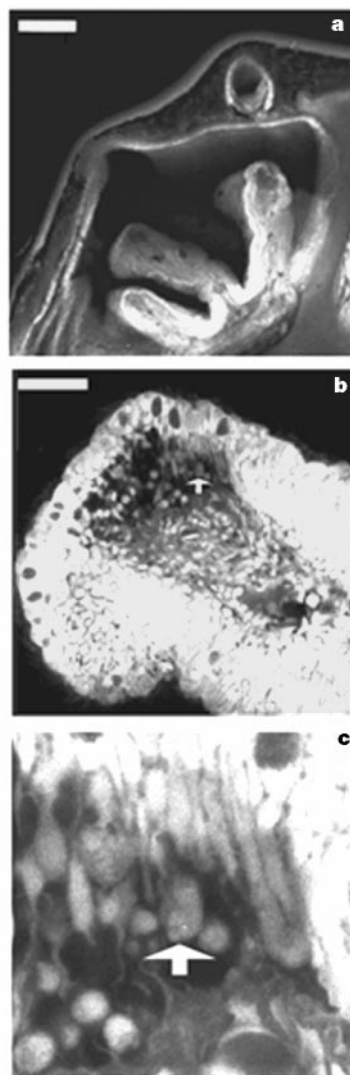


Figure 1 Step-wise increase in the magnification (CLSM autofluorescent images) of the area in the olfactory lamellae where we find magnetic crystals. **a**, Section through a trout nasal capsule with three lamellae evident within the capsule; a lateral line canal (llc) is also seen. Scale bar, 250 µm. **b**, Section through the distal half of the middle lamella in **a**, with an arrowhead pointing to the magnetoreceptor cell shown in **c**. Scale bar, 50 µm. **c**, CLSM overlay (60-µm square) taken around the magnetoreceptor cell shown in **b**. The image of the reflectance contained in the cell has been overlaid onto the autofluorescent image of the cell.

Present addresses: † Auckland Museum, Private Bag 92018, Auckland, New Zealand and § Asylum Research, 601 Pine Avenue, Santa Barbara, California 93117, USA.

sensitive to magnetic forces, it can also image magnetic structures that are covered by a layer of non-magnetic material. Both calculations and experimental results from magnetotactic bacteria have shown that MFM has sufficient sensitivity to image single-domain magnetite particles⁸. Experimentally, it has been observed that the MFM shows magnetic contrast above single-domain magnetite particles when the MFM tip is within 1 μm of the particle. To prepare the trout tissue for AFM/MFM imaging, we sectioned JB4 blocks of tissue along the z -axis until candidate particles located with the CLSM were within 100–200 nm of the block surface (Fig. 1). The location of the candidate particles was then reconfirmed and image maps generated using the CLSM to assist in precise positioning of the scanning tip of the atomic/magnetic force microscope to the same locale.

Subsequent MFM only detected a distinct ‘magnetic contrast’ at the locations where reflectance had previously been observed in CLSM (Fig. 2a, b). The areas showing magnetic contrast were less than 100 nm in diameter and had dipole moments of about 10^{-17} to 10^{-16} Ampere-metre² ($\text{A}\cdot\text{m}^2$) (Figs 2c and 3). Although the MFM image did not indicate whether the source of the magnetic contrast is a single large magnetic particle or several smaller particles, simultaneous AFM topography images showed that the magnetic sources arose from small, uniformly sized particles present either singly or in small groups (Fig. 2a).

When we applied a magnetic field, the magnetization of the particle(s) reversed. Observation of this sort of reversal in the presence of a non-zero applied magnetic field is a clear indication of magnetic hysteresis associated with ferromagnetic samples⁹. This ‘smoking gun’ (changes in polarity in a non-zero applied field) is visible in the four images of Fig. 3. The first image (Fig. 3a) shows a dark patch in the region of the magnetic source. This is consistent with an attractive interaction caused by the magnetic field from the MFM tip magnetizing the particle. The next image (Fig. 3b) was made in an applied field of +130 millitesla (mT) and shows a dipolar contrast (black/white), consistent with the magnetite particle being magnetized in the plane of the sample. This field value is below the 500-mT coercivity of the MFM tip that we used, insuring that the tip magnetization remained primarily along the axis of the tip. The two subsequent images (Fig. 3c, d) show the polarity of the imaged dipole switching in response to toggling the applied field.

We calculated the MFM image switching-field distribution

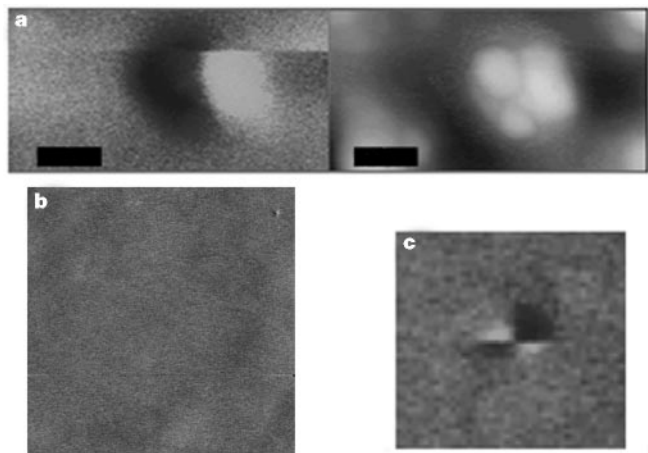


Figure 2 Images of magnetic particle(s). **a**, Scanned images of multiple particles taken simultaneously in MFM (left) and AFM (right) mode. The dipole image shown on the left is the summed field of the three particles shown on the right. Scale bar, 100 nm. **b**, MFM scan taken of a 10- μm square area in a lamella. Note the small dipole present in the upper right hand corner. **c**, MFM image (75-nm square) of a magnetic dipole switching because of the applied field of +25 mT and the field from the MFM tip.

(Fig. 4) for a particle by subtracting sequential images¹⁰. We measured a coercivity between 20 and 40 mT for the particle(s), which is consistent with measurements made on single-domain magnetite particles from magnetotactic bacteria^{10,11}. The magnetic field from the MFM tip will affect this value and therefore it must be viewed with some caution^{9,10}. Magnetite in sockeye salmon had a mean coercivity of roughly 30 mT (ref. 12), whereas the mean moment of magnetite particles extracted from the salmon was about 2×10^{-17} $\text{A}\cdot\text{m}^2$ (ref. 13). These values both agree well with observed values for the single and grouped particles shown in Figs 2 and 3 and also exclude greigite as the magnetic source. The coercivity and magnetic moment of greigite particles of the sizes found in the trout would be less than 2.5 mT and 0.5×10^{-17} $\text{A}\cdot\text{m}^2$ respectively¹⁴. In addition, we took two of the same MFM tips used on the crystals within the trout tissue and imaged magnetotactic bacteria samples. This provided a calibration sample, as the moment of the magnetite crystals within the bacteria is well defined. The calculated moment of the group of multiple crystals shown in Fig. 2 in the trout tissue using this technique is 5×10^{-16} $\text{A}\cdot\text{m}^2$, which is consistent with several single-domain-sized particles being the source of contrast in the trout images.

The reflectance of the crystals obtained on the CLSM can be mapped to a multi-lobed cell that is located within the basal lamina of a trout olfactory lamella (Fig. 5). The cell is 10–15 μm in diameter and has several processes (>4) that extend out to and are surrounded by tubular-shaped fibroblastic cells (with two processes) that help delineate the basal layer (Fig. 5a, b). Analysis of the 3D images taken in both fluorescent and reflectance CLSM mode of at least four cells gave an estimated length of the crystal chain of about 1 μm (Fig. 5c, d). The observation of single particles in AFM that are associated with the smallest magnetic sources detected in MFM thus seems likely to occur when a chain is lying end on to the surface of the block (for example, Fig. 3). Conversely, groups of particles might be observed either where the chain of

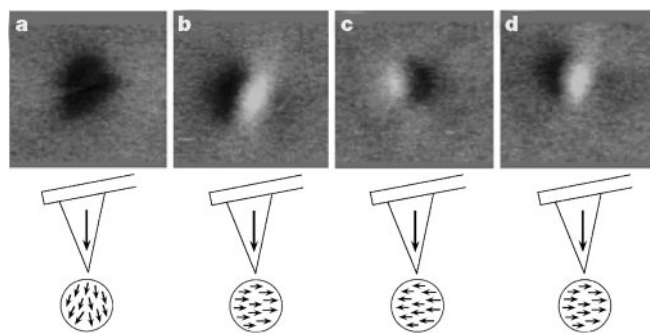


Figure 3 MFM images that show the response of a putative single magnetic particle (within trout tissue) in the presence of an applied field. The magnetic field applied in the plane of the sample was +1.4, +150, –150 and +130 mT for images **a–d**, respectively. MFM images (75-nm squares) are shown on top, with a representation of the MFM tip and magnetization of the particle underneath. The MFM tip (inverted triangle) is permanently magnetized with a coercivity of +500 mT at right angles (arrow in inverted triangle) to the applied field. The small arrows within each circle under the tip represent the alignment of the individual magnetic dipole moments that might act as the field source. **a**, Image shows a dark patch at the location of the particle. This dark patch indicates an attractive reaction between the tip and sample, consistent with the magnetic field from the MFM tip weakly magnetizing the particle and causing an attractive interaction. **b–d**, MFM images show the nearly dipolar responses of the magnetic particle under a strong applied magnetic field. These are consistent with an MFM image of a single-domain particle magnetized along the direction of the applied field. Note that the reversal of the field and dipolar response in **c** are consistent with the particle magnetization flipping in the reversed applied field. In images **b–d**, The applied field was large enough to completely align the magnetic moment of the crystals within the field.

particles bends (evident in Fig. 5c and d) or where strong attractions between opposite poles may occasionally cause aggregation of the crystals during fixation and embedding of the tissue samples.

The distinctive shape, consistent co-localization within the same sub-layer where the magnetically responsive branch of the trigeminal nerve terminates, and the presence of single-domain magnetite crystals lead us to the conclusion that these cells are excellent

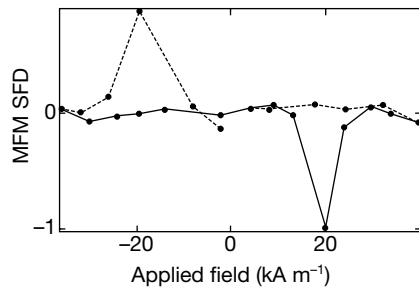


Figure 4 MFM image switching-field distribution. The switching-field distribution was measured by subtraction of sequential images of the MFM signal above the putative dipole as the applied field was systematically varied. The results were scaled to give a maximum magnitude of 1. There are two large spikes, one corresponding to a positive field value, another to a negative. The separation between the two peaks is about 40 kA m^{-1} . This implies a coercivity of 20 kA m^{-1} , consistent with values found in bacterial magnetite, also measured with an MFM¹⁰.

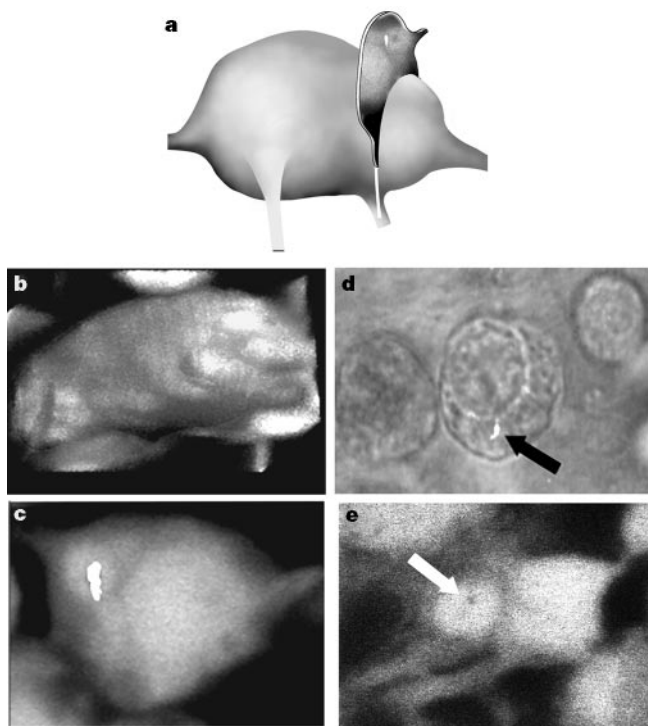


Figure 5 Images of the magnetoreceptor cell. **a**, Representation of a magnetoreceptor. A single optical slice (also shown in **c**) taken at the level of the magnetic particles is extended out of the receptor to show the placement of the magnetic particle chain. **b**, Three-dimensional volume rendered image of a single magnetoreceptor cell that shows its multi-lobed shape. **c**, CLSM optical slice overlay of an autofluorescent image of receptor and reflectance image of a $1\text{-}\mu\text{m}$ chain of magnetic particles (arrow). **d**, CLSM $30\text{-}\mu\text{m}$ wide overlay in reflected and transmitted light modes of a magnetoreceptor isolated from a trypsin digest of an olfactory lamella. The arrow indicates a chain of reflecting crystals. **e**, CLSM optical slice ($\sim 30\text{-}\mu\text{m}$ wide) taken through a magnetoreceptor within an olfactory lamella. The arrow points to the reflectance of a particle contained within the cell.

candidates for magnetoreceptors. We note that the moments for the magnetite particles extracted from the salmon suggest the chains of crystals will have a magnetic to thermal energy ratio of about four, which is consistent with their use in both the behavioural and physiological responses to magnetic fields that have been shown in a variety of taxa^{15–18}. This discovery of magnetite in a form that appears optimal for detecting changes in magnetic fields raises the possibility that magnetite is the basis of a general magnetoreceptor mechanism in taxa as distant as the vertebrates¹⁵ and arthropods^{17,19,20}. We also note that the magnetite discovered in the trout would be suitable for detecting the small changes in magnetic intensity required by a new model of magnetic position determination by homing pigeons^{21,22}. We therefore suggest that these cells are very likely to be the site of magnetic field detection in the trout and that understanding should now be sought of how the chains of crystals could transduce a magnetic field into an electrical signal in the nervous system. □

Methods

Tissue preparation

Juvenile trout (40–60 mm) were anaesthetized in 0.05% MS 222, measured and decapitated just behind the gill cover. After immersion in fixative for 24 h, the head was in embedded in JB4 resin. Thin sections were taken through the head to expose the olfactory lamellae for microscopic analysis.

Confocal microscopy

Candidate magnetic crystals were located and mapped within the lamellae using reflectance-mode on a Leica TCS 4D confocal laser scanning microscope. A combined filter set (488/568) was then used to image and map the area around the candidate crystals using tissue and glutaraldehyde induced autofluorescence. The reflecting crystals were found within single cells, and three-dimensional rendering based upon 50-nm optical slices (in both autofluorescent and reflectance mode) was done using VoxelView (Vital Images, Fairfield, Iowa) to map precisely the location of the magnetite crystal chain within a cell.

Atomic/magnetic force microscopy

A commercially available atomic/magnetic force microscope (Dimension 3100, Digital Instruments, Santa Barbara, CA) was used to generate all the images. The microscope was operated in Tapping/Lift mode, a well established technique for imaging both topography and magnetic force over a region of the sample⁹. This mode provides simultaneous high-resolution AFM images of the sample surface topography and magnetic interactions made at a well defined tip–sample separation referred to as the ‘lift height’. The imaging was done in the presence of an applied magnetic field, using a rotating rare earth magnet²³, and a high coercivity tip²⁴. This had two primary benefits: first, the applied field aligned the magnetic moment of the sample leading to stronger MFM contrast; and second, the direction of the applied field could be reversed, in turn reversing the magnetic moment of the sample and providing an unambiguous indication of the existence of magnetism in the trout tissue.

Received 3 December 1999; accepted 7 April 2000.

- Walker, M. M. *et al.* Structure and function of the vertebrate magnetic sense. *Nature* **390**, 371–376 (1997).
- Kirschvink, J. L. & Walker, M. M. in *Magnetite Biomineralization and Magnetoreception by Living Organisms: A New Biomagnetism* (eds Kirschvink, J. L., Jones, D. S. & MacFadden, B. J.) 243–254 (Plenum, New York, 1985).
- Kirschvink, J. L. & Gould, J. L. Biogenic magnetite as a basis for magnetic field detection in animals. *Biosystems* **13**, 181–201 (1981).
- Yorke, E. D. A possible magnetic transducer in birds. *J. Theor. Biol.* **77**, 101–105 (1979).
- Yorke, E. D. Sensitivity of pigeons to small magnetic field variations. *J. theor. Biol.* **89**, 533–537 (1981).
- Gould, J. L. Magnetic field sensitivity in animals. *Ann. Rev. Physiol.* **46**, 585–598 (1984).
- Kirschvink, J. L. Biogenic ferrimagnetism: A new biomagnetism, in *Biomagnetism* (eds Williamson, S. J., Romani, G. L., Kaufman, L. & Modena, I.) 501–531 (Plenum, New York, 1983).
- Proksch, R. B. *et al.* Magnetic force microscopy of the submicron magnetic assembly in a magnetotactic bacterium. *Appl. Phys. Lett.* **66**, 2582–2584 (1995).
- Babcock, K., Dugas, M., Manalis, S. & Elings, V. Magnetic force microscopy. *Res. Soc. Symp. Proc.* **355**, 311 (1995).
- Witthorn, J. *et al.* Magnetization reversal observation and manipulation of chains of nanoscale magnetic particles using the magnetic force microscope. *Nano. Mater.* **12**, 1149–1152 (1999).
- Dunin-Borkowski, R. E. *et al.* Magnetic microstructure of magnetotactic bacteria by electron holography. *Science* **282**, 1868–1870 (1998).
- Walker, M. M., Quinn, T. P., Kirschvink, J. L. & Groot, C. Production of single-domain magnetite throughout life by sockeye salmon, *Oncorhynchus nerka*. *J. Exp. Biol.* **140**, 51–63 (1988).
- Mann, S., Sparks, N. H. C., Walker, M. M. & Kirschvink, J. L. Ultrastructure, morphology and organization of biogenic magnetite from sockeye salmon, *Oncorhynchus nerka*; implications for magnetoreception. *J. Exp. Biol.* **140**, 35–49 (1988).
- Diaz-Ricci, J. C. & Kirschvink, J. L. Magnetic domain state and coercivity predictions for biogenic greigite (Fe₃S₂): A comparison of theory with magnetosome observations. *J. Geophys. Res.* **97**, 17039–

17315 (1992).

15. Semm, P. & Beason, R. C. Responses to small magnetic field variations by the trigeminal system of the bobolink. *Brain Res. Bull.* **25**, 735–740 (1990).

16. Walker, M. M. Learned magnetic field discrimination in the yellowfin tuna, *Thunnus albacares*. *J. Comp. Physiol. A* **155**, 673–679 (1984).

17. Walker, M. M. & Bitterman, M. E. Honeybees can be trained to respond to very small changes in geomagnetic field intensity. *J. Exp. Biol.* **145**, 489–494 (1989).

18. Wiltschko, R. & Wiltschko, W. *Magnetic Orientation in Animals*. (Springer, Berlin, Heidelberg, New York, 1995).

19. Gould, J. L., Kirschvink, J. L., Deffeyes, K. S. Bees have magnetic remanence. *Science* **201**, 1026–1028 (1978).

20. Lohmann, K. J. Magnetic remanence in the Western Atlantic spiny lobster. *J. Exp. Biol.* **113**, 29–41 (1984).

21. Walker, M. M. On a wing and a vector: A model for magnetic navigation by homing pigeons. *J. Theor. Biol.* **192**, 341–349 (1998).

22. Walker, M. M. Magnetic position determination by homing pigeons. *J. Theor. Biol.* **197**, 271–276 (1999).

23. Proksch, R. B., Runge, E., Hansma, P. K., Foss, S. & Walsh, B. High field magnetic force microscopy. *J. Appl. Phys.* **78**, 3303–3307 (1995).

24. Liou, S. H. & Yao, Y. D. Development of high coercivity magnetic force microscopy tips. *J. Magn. Mater.* **190**, 130–134 (1998).

Acknowledgements

We thank K. Babcock at Digital Imaging for the generous use of the AFM/MFM. The Biological Imaging Research Unit at the School of Medicine, University of Auckland, provided the CLSM and imaging facilities. In addition, we thank S. Edgar, A. Turner, H. Holloway and especially B. Beaumont for their assistance in preparation and viewing samples on the CLSM and transmission electron microscopy. Financial support came from the Marsden Fund and the School of Biological Sciences.

Correspondence and requests for materials should be addressed to C.E.D. (e-mail: cdiebel@akmuseum.org.nz) or M.M.W. (e-mail: m.walker@auckland.ac.nz).

Transformation from temporal to rate coding in a somatosensory thalamocortical pathway

Ehud Ahissar, Ronen Sosnik & Sebastian Haidarliu

Department of Neurobiology, The Weizmann Institute of Science, Rehovot 76100, Israel

The anatomical connections from the whiskers to the rodent somatosensory (barrel) cortex form two parallel (lemniscal and paralemniscal) pathways^{1,2}. It is unclear whether the paralemniscal pathway is directly involved in tactile processing, because paralemniscal neuronal responses show poor spatial resolution, labile latencies and strong dependence on cortical feedback^{3–5}. Here we show that the paralemniscal system can transform temporally encoded vibrissal information into a rate code. We recorded the representations of the frequency of whisker movement along the two pathways in anaesthetized rats. In response to varying stimulus frequencies, the lemniscal neurons exhibited amplitude modulations and constant latencies. In contrast, paralemniscal neurons in both thalamus and cortex coded the input frequency as changes in latency. Because the onset latencies increased and the offset latencies remained constant, the latency increments were translated into a rate code: increasing onset latencies led to lower spike counts. A thalamocortical loop that includes cortical oscillations and thalamic gating can account for these results. Thus, variable latencies and effective cortical feedback in the paralemniscal system can serve the processing of temporal sensory cues, such as those that encode object location during whisking. In contrast, fixed time locking in the lemniscal system is crucial for reliable spatial processing.

The lemniscal pathway of the rat trigeminal system ascends

through the ventral posterior medial nucleus (VPM) of the thalamus to the barrels in layer 4 of the cortex and to layers 5b and 6 (refs 6, 7). The paralemniscal pathway ascends through the medial division of the posterior nucleus (POm) of the thalamus to layers 1 and 5a and to the septa between the barrels in layer 4 (refs 7, 8). To reveal the processing differences between the two pathways, we recorded from single-units ($n = 710$) and multi-units ($n = 540$) of the major stations along these pathways while we stimulated (moved) the whiskers. First we analysed single- and multi-units separately. Analysis of the single-units revealed that response patterns were usually similar for neighbouring neurons. Therefore, spikes of all single- and multi-units that were recorded simultaneously from a single electrode were pooled, and these pools were referred to as ‘local populations’.

First, we examined responses to stimuli that mimic natural whisking conditions⁹: 50-ms pulses of air puffs applied to one or two rows of whiskers at 8 Hz. Typical recordings along both pathways are shown in Fig. 1. Brainstem neurons appeared simply to

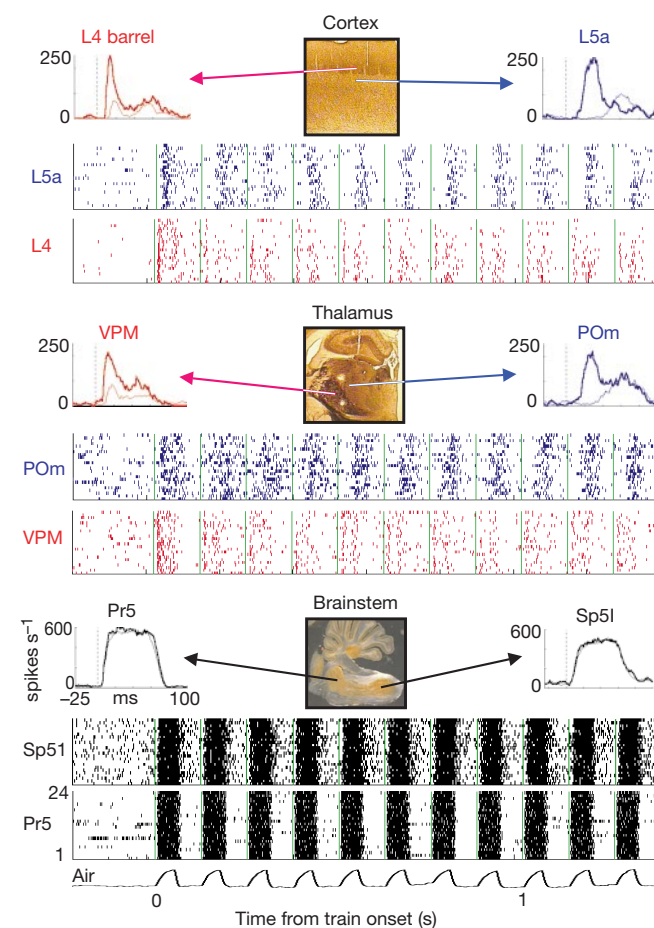


Figure 1 Lemniscal and paralemniscal thalamic transformations. Recordings of local populations from the six major stations along both pathways. Raster displays show firing times of recorded neurons (black, red or blue vertical lines) in relation to stimulus onset times (green vertical lines). Responses to 24 stimulus trains are plotted. PSTHs were computed for each stimulus cycle and are shown for the first (at time 0; thick curves) and last three cycles of the figure (cycles 9–11; thin curves). Response patterns remained steady during the remaining 13 cycles (not shown). The main trigeminal nuclei (Pr5 and Sp51) receive vibrissal input and project to both thalamic nuclei, with a bias of Pr5 towards VPM and Sp51 towards POm^{16,29}. VPM projects to cortical barrels (dark areas in layer 4) and layers 5b and 6, and receives feedback from the upper part of layer 6 (refs 6, 7, 30). POm projects to layers 1 and 5a, and the septa between the barrels in layer 4 (refs 7, 8), and receives feedback from layer 5 and the lower part of layer 6 (refs 7, 30). Electrolytic lesions in the thalamus mark recording locations of single local populations in the POm (upper) and VPM.